



Correlating structure and transport properties in pristine and environmentally-aged superionic conductors based on $\text{Li}_{1.3}\text{Al}_{0.3}\text{Ti}_{1.7}(\text{PO}_4)_3$ ceramics

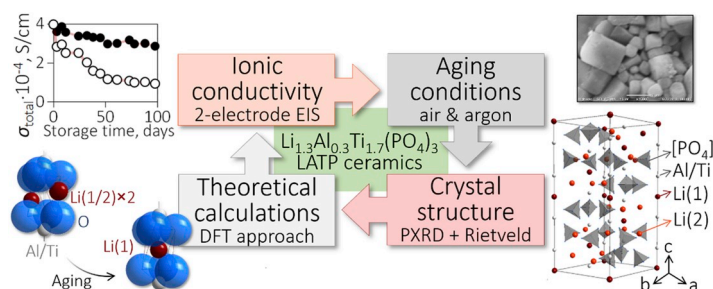
M. Pogosova^{*}, I. Krasnikova, A. Sergeev, A. Zhugayevych, K. Stevenson

Center for Energy Science and Technology, Skolkovo Institute of Science and Technology, Skolkovo Innovation Centre, 143026, Moscow, Russian Federation

HIGHLIGHTS

- Pure LATP ceramics were successfully synthesized through the solid-state approach.
- LATP total conductivity reaches $4 \cdot 10^{-4} \text{ S/cm}$ (room temperature, 18.5 vol% porosity).
- LATP undergoes structural & conductivity degradation.
- Total conductivity losses after 3-months storage: 76% (in air) 28% (in argon).

GRAPHICAL ABSTRACT



ARTICLE INFO

Keywords:

LATP
Structure–property relationship
Constitutive behavior
Aging
Microstructure

ABSTRACT

Li-ion superionic conductors play an important role in next-generation energy storage devices. To be applicable, they should meet a wide range of specifications such as safety, efficiency, affordability, and stability. The NASICON-type $\text{Li}_{1.3}\text{Al}_{0.3}\text{Ti}_{1.7}(\text{PO}_4)_3$ (LATP) compound is a well-known lithium-conductive solid electrolyte, suitable for all-solid-state and redox-flow battery prototypes offers great potential. Yet, despite the high scientific attention paid to LATP, its stability towards environmental exposure to reactive components such as water, carbon dioxide, and oxygen is poorly elucidated. Herein we evaluate under controlled conditions the structure and transport properties of LATP in both air and argon atmosphere to understand the influence of environmental processing effects over a three-month set of experiments. We demonstrate that LATP ceramics (total conductivity σ_t of $4 \cdot 10^{-4} \text{ S cm}^{-1}$ at room temperature; porosity of 18.5 vol %) degrade drastically showing 76% and 28% of the σ_t losses (for ceramics stored in the air and argon correspondingly). Based on experimental and theoretical approaches, we propose a degradation mechanism supported by Electrochemical Impedance Spectroscopy (EIS), Powder X-Ray Diffraction Analysis (PXRD), Scanning Electron Microscopy (SEM), Energy-Dispersive X-Ray spectroscopy (EDX), and Density Functional Theory (DFT) calculations.

^{*} Corresponding author. Tel.: +7 495 280 14 81x3524; Mobile: +7 909 633 28 47.

E-mail addresses: m.pogosova@skoltech.ru (M. Pogosova), i.krasnikova@skoltech.ru (I. Krasnikova), a.sergeev@skoltech.ru (A. Sergeev), a.zhugayevych@skoltech.ru (A. Zhugayevych), k.stevenson@skoltech.ru (K. Stevenson).

<https://doi.org/10.1016/j.jpowsour.2019.227367>

Received 5 July 2019; Received in revised form 25 October 2019; Accepted 29 October 2019

Available online 14 November 2019

0378-7753/© 2019 Elsevier B.V. All rights reserved.

1. Introduction

Nowadays, almost any portable electronic device contains a rechargeable lithium-ion battery. Even though commercially available Li-ion batteries have good consumer-oriented characteristics, they still have several disadvantages which hinder their larger scale adoption towards transportation and grid scale applications. For instance, such commercially available batteries can explode during the high temperature exposure, overcharge or other mechanisms due to the short-circuiting because of the Li-dendrite growth. All the issues mentioned are related mostly to the liquid form of a Li-conductive electrolyte. Therefore, the development of alternative solid-state Li-conductive electrolytes has received much current attention in realization of development of solid state battery configurations [1].

In this vein, now many are investigating Na-super-ionic-conductive (NASICON) materials that were first described in 1976 and were initially studied as superionic sodium conductors with the basic formula $\text{Na}_{1+x}\text{Zr}_2\text{Si}_x\text{P}_{3-x}\text{O}_{12}$ [2,3]. This structure is represented in two main parts: a “skeleton” that is formed by the rigid $[\text{Zr}_2\text{Si}_x\text{P}_{3-x}\text{O}_{12}]^-$ substructure, and a charge carrier Na^+ that can move within the interconnected pathways — interstitial space of the “skeleton” [2].

Later, the list of chemical elements involved into the both “skeleton” substructure and charge carrier was extended [4–6]. As the result, today the NASICON-designation corresponds more to the crystal structure family rather than the exact chemical composition or charge carrier nature.

The general formula of NASICON-type materials can be represented as: $\text{A}_{1+m}\text{M}_2(\text{BO}_4)_3$ where **A** — Li [4,7–12], Na [2–4,13], K [4]; **M** — tetravalent cation (Zr, Ti, Ge, Hf, Sn or mixture) [2–4,7–12] or its combination with trivalent cation (Al, Fe, In, Y, Ga) [4,9,10,13] or bivalent cation (Sr, Ca, Mg) [4,12]; **B** — P [2–4,7–13] or its combination with Si [4,9]. Therefore, the amount of a charge carrier **A** can be modified by changing the overall charge of a “skeleton”.

The NASICON crystal structure family includes four polymorph modifications [10,14]:

- α — rhombohedral, $R\bar{3}c$ space group;
- α' — triclinic, $P\bar{1}$ space group;
- β — orthorhombic, $Pbna$ space group;
- β' — monoclinic $P2_1/n$ space group;

As established previously, the α -NASICONs demonstrate higher Li-conductivity in comparison with other polymorphs [6,10,14]. Therefore, many studies are focused on the stabilizing of α -polymorph modification under the exploitation conditions used [10].

Within the wide list of all the Li-conductive NASICON-type compounds, the $\text{Li}_{1+x}\text{Al}_x\text{Ti}_{2-x}(\text{PO}_4)_3$ (LATP) based materials seem to be the most promising for further optimization: Ge-substituted LATPs were shown to possess the highest values of total conductivity σ_t within the NASICON family which reaches $1.5\text{--}5 \cdot 10^{-3} \text{ S cm}^{-1}$ [5,15,16]. Nevertheless, it was reported that aging in air leads to decrease in the transport properties [15]. Hence, chemical stability and durability influence the key characteristic of a solid Li-conductive electrolytes i.e., ionic conductivity. Thereby, a deeper analysis of parental LATP compound is required for better understanding of a degradation process to form a better optimization of its performance at future.

The x values of $\text{Li}_{1+x}\text{Al}_x\text{Ti}_{2-x}(\text{PO}_4)_3$ influence the total conductivity. It was established, that the optimal chemical composition of LATP that performs with the highest conductivity is $\text{Li}_{1.3}\text{Al}_{0.3}\text{Ti}_{1.7}(\text{PO}_4)_3$. The explanation of Al-content optimum existence is usually based on the combination of two factors with opposite effect [6,8,17–20]:

- Conductivity increases when the charge carrier amount increases;
- Conductivity decreases when the number of Li-vacancies necessary for a successful Li^+ migration decreases;

Thereby, the $\text{Li}_{1.3}\text{Al}_{0.3}\text{Ti}_{1.7}(\text{PO}_4)_3$ chemical composition was chosen to be investigated in the current work.

The synthesis of LATPs can be carried out via wide range of methods: coprecipitation with subsequent calcination, glass-ceramic synthesis, solid-state synthesis, etc. Many morphological issues can be solved through the optimization of synthesis conditions [17–21]. Taking into account the importance of the chemical composition strict control and the possibility of thorough Powder X-Ray Diffraction (PXRD) based crystal structure analysis (that requires micro-sized crystallites), a solid-state synthesis approach was chosen to be applied in the current study.

In spite of many LATP-based studies, the amount of thorough investigations that include a combination of both analytical and theoretical approaches is rather limited. In addition to this, the stability of LATP towards the aging has not been fully detailed and as such many contradictory claims [14,18,21] have been made that leads to misunderstanding. Therefore we designed a set of studies using a full analytical routine including the structural (PXRD and PXRD-based Rietveld refinement), electrochemical (Electrochemical Impedance Spectroscopy — EIS), morphological (Scanning Electron Microscopy — SEM), and elemental characterization (Energy-Dispersive X-ray spectroscopy — EDX) to be able to correlate structural and transport properties of LATP of both pristine samples and aged samples after exposure to ambient conditions. In addition to the classical analytical characterization, a computational Density Functional Theory (DFT) based approach is used to understand and interpret experimental observations. These calculations proved to be useful for investigation of the ion migration mechanisms in solid electrolytes, particularly, the significance of the concerted motion of ions [22,23], and to estimate the migration barriers for both vacancy and interstitial migration [24]. Furthermore, our DFT calculations allow us to propose a new low energy lithium position $\text{Li}(1/2)$ involved in the interstitial migration which was not described before [24]. Therefore, we can expect this work to be important for fundamental aspects of Li-ion conductivity of LATP as well as for applied implementations to explain its performance as a superionic conductor. Furthermore, we may expect our study to be useful for the optimization of LATPs application and storage conditions, which, in its turn, will likely improve the final outcome.

2. Experimental

2.1. Synthesis

The reagent-grade Li_2CO_3 , $\text{Al}(\text{NO}_3)_3 \cdot n\text{H}_2\text{O}$, TiO_2 , $(\text{NH}_4)_2\text{H}_2\text{PO}_4$ were used. The solid-state synthesis was carried out using the Nabertherm L5/12/P330 muffle furnace and the Hydraulic press Platen Press P 300 P/M. Since, aluminum nitrate $\text{Al}(\text{NO}_3)_3 \cdot n\text{H}_2\text{O}$ has variable chemical composition (n), this reagent was preliminarily decomposed to Al_2O_3 to provide the correct stoichiometry of LATP. The alumina was prepared by a thermal decomposition of reagent-grade $\text{Al}(\text{NO}_3)_3 \cdot n\text{H}_2\text{O}$ (heating up to 900°C , holding for 2 h). Fresh Al_2O_3 was taken out of the hot furnace (air quenched), cooled naturally, and then mixed with other compounds in stoichiometric proportions to obtain ca. 5 g of the final $\text{Li}_{1.3}\text{Al}_{0.3}\text{Ti}_{1.7}(\text{PO}_4)_3$ compound. The reagent mixture was thoroughly manually ground in an agate mortar. Then, the powder obtained was pressed into pellets (1 cm diameter press-form is; 33 Bar pressure applied on the working piston). After, pellets were placed in an alumina crucible, which was subsequently put into the muffle furnace. The solid-state synthesis was then carried out as follows:

1. Heating for 2 h up to 250°C (holding for 2 h) with subsequent heating for 2 h up to 725°C (holding for 2 h) and further heating for 1 h up to 750°C (holding for 6 h). Afterwards, the sample was quenched. The porous chunk obtained was then ground thoroughly in agate mortar. The powder received was pressed into pellets

~250 mg each (1 cm diameter press-form is; 33 Bar pressure applied on the working piston);

2. Heating for 2.5 h up to 850 °C (holding for 6 h) with subsequent air quenching. After cooled naturally, all pellets obtained were put into the argon-filled GloveBox immediately.

Final pellets are ready to be prepared for further EIS, SEM, and EDX. To implement the powder X-Ray diffraction (PXRD) analysis ceramic pellets were ground manually in agate mortar to fine powder.

2.2. Phase and structural analysis

The PXRD patterns were registered using the Bruker D8 Advance ($\text{CuK}\alpha_{1,2}$ radiation; LynXeye XE detector; 2.5° soller slits; 1 mm fixed divergence slit; 30° min⁻¹ sample holder rotation; 2θ range from 10° to 120°; 2θ step = 0.01°). The PXRD patterns intensities exceed 150 000 counts. Crystal structure of the obtained compounds was refined by the Rietveld method in the $R\bar{3}c$ space group using the JANA 2006 software [25].

The LeBail refinement settings, zero shift, and asymmetry factors were established by the registration, profile and structural analysis of the Al_2O_3 NIST 676a standard [26]. The Al_2O_3 refinement results are given in Supplementary, Section 1. As a result, the final LeBail refinement settings were as follows: background — manual in combination with the Chebyshev polynomial with 5 variables; unit cell dimensions a and c ; profile — Pseudo-Voigt peak-shape function with GW , LY , LX , Lxe ; zero-shift (values of the alumina standard were input and fixed); vertical shift — Sycos; asymmetry — by divergence with HpS/L (values of the alumina standard were input and fixed).

The structure refinement parameters were as follows: atomic positions of Al, Ti, P, and O (the starting atomic positions were taken from Ref. [27]; Al and Ti shared a joint position; Li positions were fixed); thermal displacement parameters — harmonic anisotropic approximation for Al and Ti, isotropic approximation for P, O, and Li (fixed for the latter one). All occupancies were fixed on the nominal values. The samples that came through the PXRD-based structure refinement will be further denoted as AirN and ArN for air- and Ar-stored samples respectively, where N is serial number.

2.3. Li-ion conductivity analysis

Gold electrodes (30 nm thickness; 8 mm diameter) were sputtered on both plane faces of the pellet using the magnetron-sputtering machine Quorum Q150T ES and the 8 mm diameter mask. The EIS results were registered using a two-electrode cell with copper electrodes. The masks, impedance cell, and copper electrodes were designed using the FreeCad software [28] and fabricated through PLA using the Ultimaker 2+ 3D printer and the HAAS DM-1 CNC Drill/Mill center (Figure A2, Supplementary, Section 2). The project files (in.stl and .step format) of masks, cell and electrodes used are available at Mendeley Data (<https://doi.org/10.17632/23hkrycsbw.1>; please, refer to this article if used).

Impedance studies were carried out at a galvanostat/potentiostat Metrohm Autolab (frequency range 1 MHz–10 Hz, amplitude 10 mV vs Root Mean Square (RMS)). For each experiment, at least 5 spectra were recorded, approximation was carried out using the original Metrohm Autolab NOVA software. A quality of data was verified using Kramers-Kronig Relations ($X^2 \sim 10^{-5}$ – 10^{-6}). EIS data were recorded in a temperature T range from –160 to +60 °C. Samples were exposed to low temperatures using a liquid nitrogen (T was checked by the Testo 735 multichannel thermometer with the Testo Type K chromel-alumel thermocouple probe), while the 5–60 °C range was supported by the TSO-1/80 SPU thermostat.

A relative error in conductivity measurement was estimated to be 6% for σ_b and 5% for σ_{gb} , σ_t , and C_{gb} . A relative error values were estimated using approach for indirect measurement taking into account error of

Nova approximation (less than 5%) and errors of direct measurements of the samples thickness and diameter (Supplementary, Section 3).

Activation energy of conductivity was calculated from Arrhenius type plot using the following formula:

$$\sigma \cdot T = \sigma_0 \cdot \exp(-E_a/RT)$$

Error in the E_a calculation was estimated from graphical data (least square linear fit — the standard error value for the constant k for a linear function $y = kx + b$ which was obtained using the LINEST approximation in Excel) to be 0.004, 0.02 and 0.01 eV for bulk, grain boundary and total E_a , correspondingly.

2.4. Degradation experiment — electrochemical and structural properties

One pellet with electrodes deposited was stored in the air (room temperature). Another similar pellet was stored in the dried argon atmosphere in the Siemens MBraun 200 B ECO GloveBox (average temperature 25 °C; overall pressure < 0.4 mbar; partial pressures: P_{O_2} < 10 ppm; $\text{P}_{\text{H}_2\text{O}}$ < 10 ppm). Both pellets were regularly analyzed via EIS to define the Li-ion conductivity changes that can appear through the aging in different atmospheres.

To examine the structural changes occurred during the aging in air a powder sample was deposited on the PXRD sample holder and stored in air in a plastic Petri dish (room temperature). To investigate the aging in argon, a pellet was taken out from the GloveBox right before the PXRD experiment that includes grinding in an agate mortar and immediate PXRD registration. PXRD measurements were carried out approximately once a month.

2.5. Morphological and elemental analysis

To analyze the morphology of ceramics obtained, a scanning electron microscopy (SEM) was carried out using the Jeol JCM 6000 microscope. To determine the grain size distribution different areas of ceramics were explored and more than 200 grains were taken into consideration. To examine the intergranular changes the focused ion beam (FIB) SEM was carried out on the FEI Osiris microscope operated at 200 kV and equipped with a super-X detector, followed by the EDX mapping of the heaviest element — titanium. The Al:Ti ratio was estimated through the energy-dispersive X-ray spectroscopy (EDX) implemented by the scanning electron microscope Jeol JSM-6490LV (W-cathode, operating at 30 kV) equipped with the EDX system INCA Energy+ (Oxford, Si-(Li)-detector).

2.6. Density Functional Theory calculations

The DFT calculations were performed with the help of the Vienna ab initio Simulation Package (VASP) [29] using the PBE generalized gradient approximation (GGA) functional [30] and projector augmented wave (PAW) pseudopotentials [31] to describe core electrons. Plane wave basis set cutoff was set to 500 eV. The k -points were generated with a spacing not larger than 0.235 Å⁻¹ along the axes of the reciprocal unit cells. Minimum energy path (MEP) calculations were performed using the nudged elastic bands technique (NEB) [32]. All the VASP calculations were automated with the help of SIMAN package [33].

The orthorhombic simulation cell used in the calculations containing 4 formula units of LTP (i.e. $\text{LiTi}_2(\text{PO}_4)_3 \times 4$) was obtained by transformation matrix [0 1 0; -1 0 1; 1 -1 1] from the primitive rhombohedral cell (or [-1 1 1; -3 -3 0; 2 -2 1]/3 from hexagonal cell). Its shape and volume as well as the ionic positions were relaxed. The final dimensions of the cell were: 8.68 × 8.65 × 12.26 Å. For the LATP MEP calculation the cell was duplicated along the orthorhombic c -axis so that its length became 24.45 Å and it contained a straight diffusion path consisted of four **Li(1)** positions. One of the Ti atoms was replaced by Al atom. The ion positions of the NEB images were relaxed until the maximum force

acting on the atoms was less than $0.05 \text{ eV } \text{\AA}^{-1}$.

3. Results

3.1. Phase composition

The main NASICON phase formation was studied using step-by-step PXRD phase analysis (Figure A3, Supplementary, Section 4). The sharp peak shape identifies that the material obtained is well-crystallized and the crystallites are expected to be micro-sized. It is seen, that the NASICON phase forms mainly after the first annealing step (with final temperature 750°C). In addition to the main phase peaks, weak but well-resolved reflexes can be distinguished easily (Figure A4, Supplementary, Section 4). These reflexes are attributed to the same main LATP phase and caused by the residual low-intensity X-Ray irradiation, namely CuK_β and $\text{WL}_{\alpha 1}$ (Figure A4, Supplementary, Section 4) [34]. Therefore, the materials synthesized are pure and contain the target LATP phase only.

3.2. Crystal structure features

The experimental, refined and differential PXRD patterns for all samples are given in Supplementary, Section 5 (Figure A5–A9). The selected results of Rietveld refinement are given in Table 1. The particular crystallographic data for all samples are presented in Supplementary, Section 5 (Table A1–A5).

The true density (ρ_{true} , g cm^{-3}) values obtained were used further for the calculation of ceramics porosity (see Table 1; Supplementary, Section 6).

Table 1

Characteristics of the sample degraded on air and argon: R -factors (R_{wp} , R_p , $R_{\text{f}}^{\text{all}}$, $R_{\text{B}}^{\text{all}}$), unit cell dimensions (a , c , and V), the CCDC database number (CCDC #), true density (ρ_{true}), estimated porosity (%), average grain size (μm) intra-structural polyhedron volumes ($[\text{MO}_6]$, $[\text{PO}_4]$, $[\text{Li}(2)\text{O}_6]$, and $[\text{Li}(1)\text{O}_6\text{M}_2]$)¹, aging duration (τ , days), and approximate total conductivity (σ'_t , S cm^{-1})². All errors are given in estimated standard deviations (e.s.d.).

Estimated porosity — 18.5%

Average grain size — $0.9(3) \mu\text{m}$.

	Ar1	Ar2	Air 1	Air 2	Air 3
τ , days	42	67	4	34	66
R_{wp}	9.12	8.30	9.61	8.80	9.16
R_p	5.97	5.51	6.43	5.44	5.56
$R_{\text{f}}^{\text{all}}$	3.60	3.40	3.38	3.07	3.36
$R_{\text{B}}^{\text{all}}$	5.85	5.40	5.41	4.96	5.47
a , \AA ^c	8.4991(1)	8.4988(1)	8.4985(1)	8.5006(1)	8.5006(1)
c , \AA ^c	20.8376	20.8316	20.8212	20.8070	20.8061
	(3)	(3)	(3)	(2)	(2)
V , \AA^3 ^c	1303.54	1303.06	1302.33	1302.09	1302.03
	(2)	(2)	(2)	(2)	(2)
CCDC #	1 883 402	1 883 403	1 883 399	1 883 400	1 883 401
ρ_{true} , g cm^{-3}	2.9306(1)	2.9317(1)	2.9333(1)	2.9339(1)	2.9340(1)
$[\text{MO}_6]$, \AA^3 ^a	9.30(3)	9.34(3)	9.31(3)	9.33(3)	9.31(3)
$[\text{PO}_4]$, \AA^3 ^d	1.86(2)	1.85(2)	1.85(2)	1.85(2)	1.86(2)
$[\text{Li}(2)\text{O}_6]$, \AA^3 ^d	12.36(1)	12.40(1)	12.39(1)	12.34(1)	12.34(1)
$[\text{Li}(1)\text{O}_6\text{M}_2]$, \AA^3 ^d	15.80(1)	15.79(1)	15.79(1)	15.70(1)	15.69(2)
σ'_t , S cm^{-1} ^b	3.3	3.1	2.9	1.9	1.1

^a M — crystallographic position, occupied by Al and Ti.

^b The σ'_t values were calculated using the linear approximation of the degradation plots, please see the Discussion, Section 4.5 and Supplementary, Section 13.

^c The error values were calculated via Jana2006 software.

^d For more details regarding polyhedral volumes and error calculations, please, see the Discussion, Section 4.5 and Supplementary, Section 14.

3.3. Temperature dependence of the Li-ion conductivity

The Nyquist plots recorded at different temperatures are presented in Fig. 1.

It is seen that the temperature influences strongly the Nyquist plot patterns (Fig. 1): at -160°C we observe only one distorted semicircle (Fig. 1a); at -100°C two separate semicircles (Fig. 1b); at room temperature we see one semicircle and a “tail” which is usually attributed to electrode polarization (Fig. 1d) [35]. The temperature evolution of bulk and grain boundary resistance is given in Table A6, Supplementary, Section 7.

The temperature dependence of conductivity (Arrhenius plots) is given in Figure A10, Supplementary, Section 8. Basing on these plots, the activation energies E_a of bulk, grain boundary, and total conductivity were estimated to be 0.186 ± 0.004 , 0.46 ± 0.02 and $0.37 \pm 0.01 \text{ eV}$, respectively.

3.4. Li-ion conductivity as a function of storage time and atmosphere

Fig. 2 depicts the behavior of bulk, grain boundary and total conductivity and capacitance of samples which were stored in air and Ar atmospheres.

As it is seen from the plots in Fig. 2, conductivities of the samples stored both in air or Ar atmosphere decrease with the storage time. However, it is necessary to underline, that the conductivity deterioration behavior depends strongly on the storage atmosphere. In terms of Li-ion conductivity, the Ar-stored samples possess definitely higher stability towards aging in comparison with the air-stored samples: the σ_b , σ_{gb} , and σ_t values decrease by 10, 33, and 28% respectively in case of the aging in the Ar atmosphere, and by 25, 80 and 76% respectively in case of the aging in the air atmosphere.

3.5. Morphology and elemental analysis

Fig. 3a,b represent microphotographs of the sample that had been stored in air. It is seen that the grains are well defined and have a polyhedron shape. The average particle size was established to be $0.9 \pm 0.3 \mu\text{m}$ (the grain size distribution plot is given in Figure A11, Supplementary, Section 9). Fig. 3c,d shows the cross-section microphotographs and EDX-based Ti-mapping of the pellets stored in air and argon atmospheres for over than 100 days. It is clearly seen that the air-stored sample shows wider intergranular edges than the Ar-stored sample that has almost invisible intergranular edges (except the micropores incorporated).

Figure A12 (Supplementary, Section 10) represents microphotographs of the sample that has been stored in air. EDX-analyzed areas are marked with borders and the Spectrum N labels, where N is a sequential number. The Al:Ti atomic ratio was established to be $0.26(2):1.7(2)$. The particular numerical data are given in Table A7 (Supplementary, Section 10).

4. Discussion

4.1. The LATP-phase formation

In accordance with the step-by-step PXRD phase analysis (Figure A3, Supplementary, Section 4) the final pristine material obtained represents the most conductive α -NASICON LATP phase only. Analyzing the microphotographs of the final ceramics (Fig. 3) we found no visible melt incorporations. Thus, we can assume the absence of amorphous glass-like impurities which cannot be detected through the PXRD method. Therefore, we can further discuss the material obtained as pristine. Considering the sharp and well-resolved peaks of PXRD pattern we pointed out that the material obtained is well-crystallized with micro-sized crystallites. This assumption agrees with the SEM results, based on which we established the highly crystallized grain shape behavior

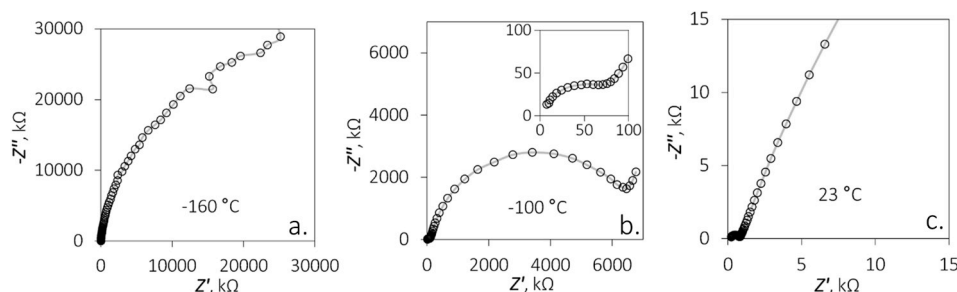


Fig. 1. Nyquist plots collected at -160 (a.), -100 (b.; the high frequency range of 1 MHz–1.5 kHz — inserted), and 23 (c.) °C.

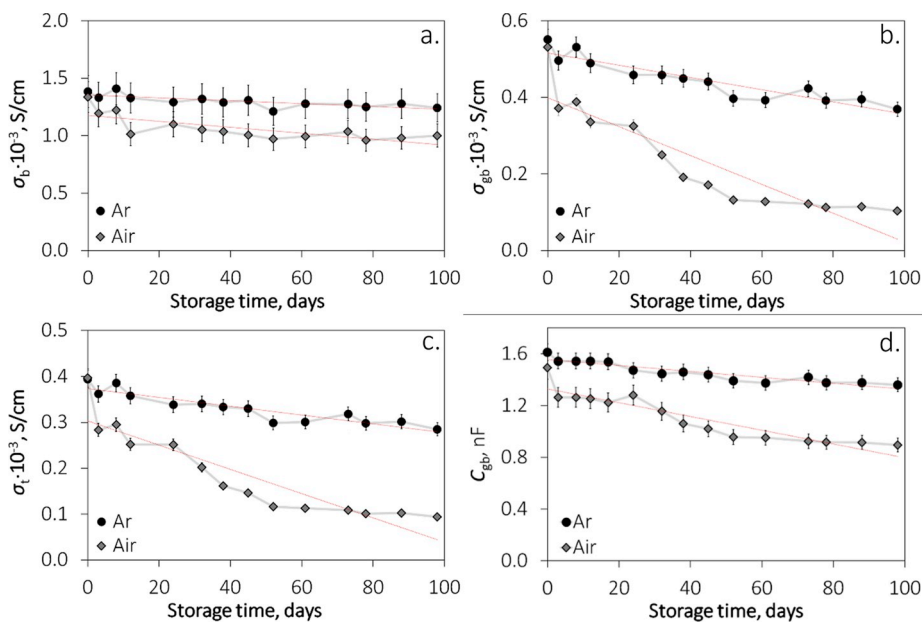


Fig. 2. The LATP conductivity and capacitance changes observed during the storage in air and in Ar: bulk conductivity (a), grain boundary conductivity (b), total conductivity (c), capacitance (d). Line is only used to show trend.

(well-defined polyhedrons) and the mean grain size of $1 \mu\text{m}$. Taking into account the consequences mentioned above, we conclude the synthetic approach used is suitable for a fast formation of the high quality α -NASICON-based LATP ceramics.

4.2. The LATP crystal structure — aging behavior

Assuming the LATP and Al_2O_3 ceramics X-Ray absorption coefficients are approximately similar and taking into account the same diffractometer used in all cases, we decided to apply the zero-shift and asymmetry factors obtained after the Al_2O_3 NIST 676a standard Rietveld refinement routine (see Supplementary, Section 1) to the LATP refinement procedure.

Based on a thorough analysis of the peak position shifts and in accordance with the sample preparation features (small amounts of the sample powder were deposited on the sample holder's flat side with no strict height control provided), we decided to involve the vertical shift correction into the refinement algorithm.

In accordance with the EDX results and taking into account the limitations of PXRD (small Al content and negligible difference of the electronic density between Al^{3+} and Ti^{4+} ions; low electronic density of Li^+ ions) we decided to fix the nominal occupancies of Al, Ti, and Li. In addition to this, we followed the $[\text{PO}_4]$ -constancy approximation and, therefore, fixed P and O occupancies either. As a result, we refined the structures obtained considering the chemical composition to be nominal.

LATP belongs to the rhombohedral $R\bar{3}c$ space group that corresponds to the α -polymorph modification of the NASICON crystal structure (Fig. 4) [27]. The “skeleton” of LATP is built of $[\text{MO}_6]$ octahedrons (where M denotes the 12c position, occupied by Al and Ti), and $[\text{PO}_4]$ tetrahedrons. In accordance with [27], Li-ions occupy two separate positions:

6b, that will be further denoted as Li(1);

36f, that will be further denoted as Li(2);

It was shown that the variation of aluminum content x influences the occupancy of Li(2) position. When $x = 0$ all lithium is located in Li(1) position. The substitution of Ti^{4+} by Al^{3+} increases the overall negative charge of the “skeleton”, that allows the additional Li^+ ions to enter the structure and occupy the Li(2) position [27].

We applied the anisotropic approximation of thermal displacement parameters for the heaviest M position only (Al, Ti). In accordance with the low content of Li^+ and its low electronic density, we decided to fix thermal displacement parameters for the Li(1) and Li(2) positions. We refined the thermal displacement parameters of remaining positions in isotropic approximation.

Carrying out several PXRD analyses we found out that the unit cell dimensions change evidently with time (Table 1). Therefore, we can maintain that the pure LATP ceramics degrade and these degradation processes involve structural changes that can be detected via PXRD-based structure refinement. Studying these changes thoroughly we established that the unit cell volume V decreases with aging time (Table 1; Figure A13a, Supplementary, Section 11). It is seen that the

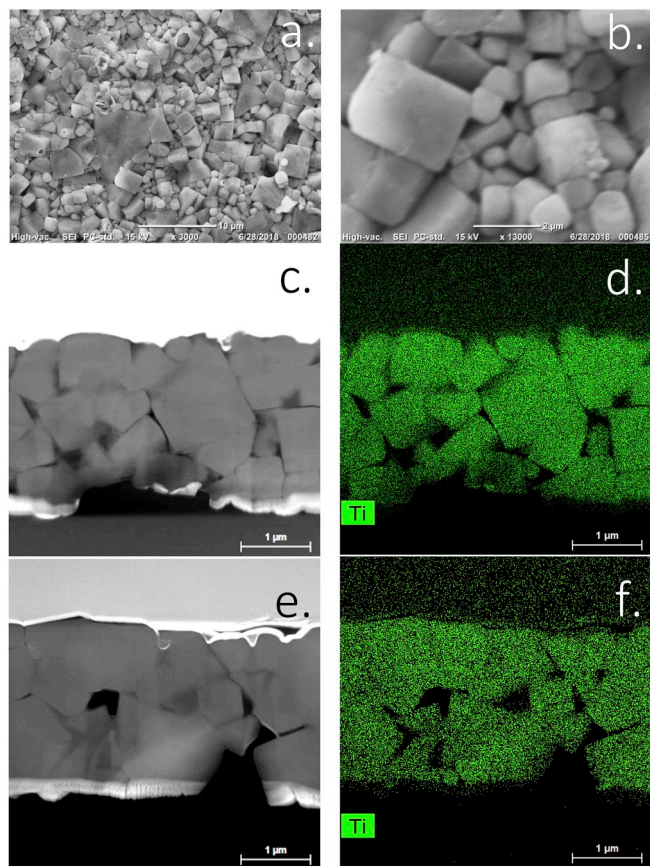


Fig. 3. Microphotographs of the pellet stored in air: $\times 3000$ magnification (a) and $\times 13\,000$ magnification (b) and the cross-section microphotographs and EDX-based Ti mapping of a pellet stored in air (c, d) and in argon (e, f).

decrease of c axis makes the main impact while the a axis changes are insignificant (Table 1; Figure A13b, Supplementary, Section 11). The structural changes in solid solutions with complex crystal structure typically possess similar behavior: ambiguous changes of unit cell dimensions and clear unit cell volume trend [36]. Therefore, we can assume the anisotropic changes of unit cell dimensions.

4.3. Equivalent circuit verification

Despite EIS of LATPs is well described in literature, the interpretation of results described, especially in terms of the equivalent circuit correspondence, is ambiguous [15,20,37–40]. Therefore, we decided to start the electrochemical characterization of the materials obtained with the equivalent circuit verification.

It was found that the Nyquist plot registered at room temperature

(Fig. 1c) is well described with the following equivalent circuit: $R_1(R_2C_2)CPE$ (error of approximation did not exceed 5%). In literature, R_1 is either attributed to the resistance between electrode and sample or to the bulk resistance [7,41]. From the work of Bauerle [42] it is known that polycrystalline ceramic material is well described by the $(R_bC_b)(R_{gb}C_{gb})(R_{el}C_{el})$ scheme, where R_bC_b stands for bulk resistance and capacitance, $R_{gb}C_{gb}$ — grain boundary values, $R_{el}C_{el}$ — effects from electrode. Frequently, in case of LATP/LAGP materials, a grain conductivity is too high to be registered within the ordinary frequency range used for EIS technique at room temperature and only one semicircle can usually be observed [43]. Taking into account the ion conductivity behavior that fades with the temperature decrease, it is expected that the lower EIS measurement temperature increase the R_b and, therefore, makes the first semicircle visible on the Nyquist plot [38,41]. Thus, the low-temperature-EIS may be considered as a scheme-verification approach.

As it was shown before, the EIS measurement at -160°C shows one semicircle only (Fig. 1a), while the measurement at -100°C clearly reveals the appearance of 2 semicircles that evidently correspond to the bulk (at higher frequencies) and grain boundary component (Fig. 1b). Apparently, it shows that the bulk-related semicircle shifts towards higher frequencies along with the temperature growth and, therefore, becomes undetectable under the room temperature conditions (Fig. 1c). Therefore, the low-temperature EIS experiment provided proves that in the $R_1(R_2C_2)CPE$ circuit R_1 stands for a bulk conductivity, while R_2 and C_2 are attributed to grain boundary resistance and capacitance (considering that no phase changes occur in the range of -100 – $+60^\circ\text{C}$).

4.4. Li-ion conductivity changes

The conductivity values of as-prepared sample were as follows: $\sigma_b = 1.39 \cdot 10^{-3} \text{ S cm}^{-1}$, $\sigma_{gb} = 5.5 \cdot 10^{-4} \text{ S cm}^{-1}$ and $\sigma_t = 3.95 \cdot 10^{-4} \text{ S cm}^{-1}$ (for the bulk, grain boundary, and total conductivity correspondingly, room temperature, 81.5% density). In recent article, Hallopeau claimed that $3.15 \cdot 10^{-4} \text{ S cm}^{-1}$ is a high value of conductivity at given density (88%) in comparison to other works [44]. Therefore, the results obtained in current work could be considered as competitive.

As it was shown before, a conductivity of the samples stored in Ar and air atmosphere gradually decreases (Fig. 2). While it is known that NASICON type material may react with moisture from air [15], an effect of aging in Ar may be attributed to minor H_2O , CO_2 and O_2 concentrations, that could be presented within an Ar-filled GloveBox (according to the Ar supplier, gas contains 0,002 vol% O_2 ; 0,003 vol% H_2O vapour; 0,00002 vol% CO_2).

Reference sample (ceramic pellet with no Au electrodes sputtered) was stored within a GloveBox and it was shown that its conductivity coincide with the data obtained for sample stored under the same conditions but with Au electrodes sputtered (Fig. 2). Therefore, it was proven that Au electrodes do not affect the aging behavior under the conditions mentioned. Hence, one may expect that the magnetron

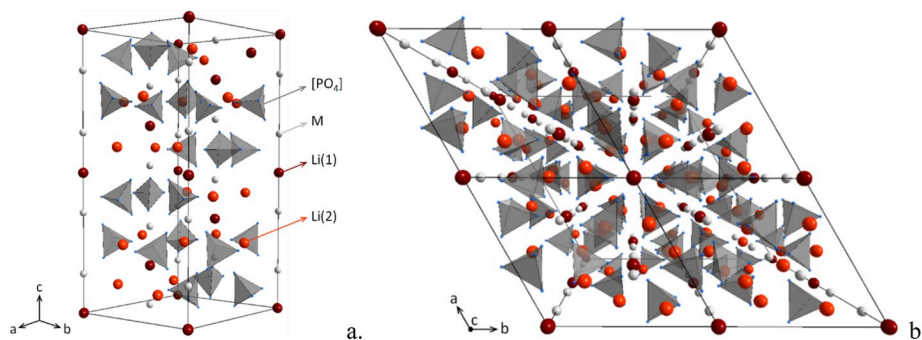


Fig. 4. The LATP crystal structure: one unit cell, side view (a) and 4 unit cells, top view (b). The M designation marks the Al/Ti shared position.

sputtered gold electrodes do not cause any changes of the LATP ceramics during the storage. In both cases, grain boundary conductivity σ_{gb} deteriorates more significantly than bulk conductivity σ_b . Observed tendency lays in a good agreement with literature data for LAGTP materials [15].

Since EIS data were well described with $R(RC)CPE$ equivalent circuit it was possible to track the changes of a grain boundary capacitance (Fig. 2d). For the sample stored inside a GloveBox capacitance remained almost the same (only 12% decrease) while storage in air resulted in 40% deterioration of capacitance. This effect may be related to the growth of grain boundary layer.

According to Dijk, thickness of grain boundary is inversely proportional to capacitance values C [45]. Taking into account formalism developed in works of Dijk [45] and Marriapan [38] and making several assumptions, we derived a formalism that allows making a rough estimation of thickness of the grain boundary layer (Fig. 5, Supplementary, Section 12).

While the thickness of grain boundary layer of sample stored in Ar remains the almost same (from 13 to 16 nm), we can see that the grain boundary layer of sample stored in air increases almost twice (from 15 to 25 nm). This trend corroborates with the SEM-FIB data given above (Fig. 3) where the growth of space between grains is clearly seen.

4.5. Correlations between the crystal structure and conductivity

As described in the Introduction, crystal structure features influence strongly the conductivity properties of the solid-state NASICON-based Li-conductive electrolyte. Analyzing the evident changes of LATP caused by the aging processes, we studied the structure-conductivity dependency.

We compared the changes of unit cell volume V and total conductivity σ_t that both decrease with storage time. We decided to study the three-dimensional parameter V as it is considered to be an integral operator: V changes represent a summarized impact of all unit cell dimension variations. It is worth to mention that PXRD and EIS data were not collected simultaneously. To compensate for this fact, we estimated values of the total conductivity σ_t using the linear approximation of σ_t fading dependencies (Figure A14, Supplementary, Section 13). This approach allows us to normalize the degradation impact on crystal structure and conductivity.

As it is shown in Fig. 6, V and σ_t values do correlate, but the correlation observed is weak and shows the overall tendency only that Li-ion conductivity falls with the unit cell volume decreases.

Taking into account that V can be discussed as the combination of intracell polyhedral units, we decided to investigate the intrastructural polyhedrons volumes behavior. Similarly to the V interpretation, we consider the polyhedron volume as an integral operator that represents interatomic distances and relative positions. The polyhedra studied are as follows: $[PO_4]$ tetrahedron, $[MO_6]$ octahedron, $[Li(2)O_6]$ deformed octahedron, and $[Li(1)O_6M_2]$ bi-pyramidal antiprism (corresponds to

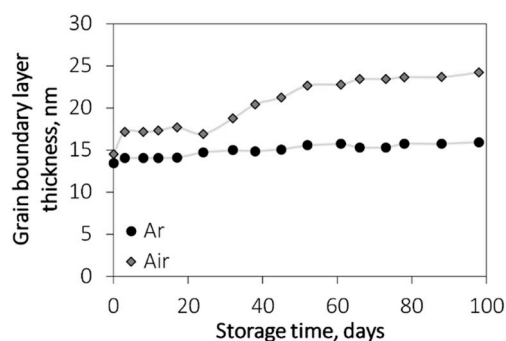


Fig. 5. Estimative changes in grain boundary thickness of LATP during storage in air and in Ar (23 °C).

V_{poly}). All polyhedra discussed are illustrated in Fig. 6c. Detailed information regarding the polyhedral definition and volumes calculation is given in Supplementary, Section 14.

As it was described before, we found out that aging leads to the dramatic changes in c dimension of the unit cell. Carrying out a deeper structural analysis, we figured out the changes of $M-Li(1)-M$ interatomic distances. Taking into account that both M and $Li(1)$ atomic positions are laying on the c axis and expecting a strong influence of the Al^{3+}/Ti^{4+} electrostatic cation field on Li^+ (that may cause the conductivity changes), we decided to include the M positions into the $Li(1)$ polyhedron. Therefore, this kind of $Li(1)$ polyhedron considers additionally the $M-Li(1)-M$ distance changes. All polyhedrons volumes calculated are presented in Table 1.

Analyzing the dependencies of polyhedral volumes on the aging time and atmosphere, we established distinguishable changes in case of $Li(1)$ polyhedron (Table 1) while the volumes of other polyhedrons remained almost the same (Figure A17, Supplementary, Section 15).

Comparing the aging behavior of V_{poly} with σ_t we noticed their similarity and decided to investigate the correlation between these two independent LATP characteristics. As a result, we found out a good 95% correlation between V_{poly} and σ_t (Fig. 6b; Figure A18, Supplementary, Section 16).

As it was mentioned before in Introduction, the parental $LiTi_2(PO_4)_3$ (LTP) compound initially contains lithium at the $Li(1)$ position that is occupied fully. Thereby, the Al-doping of LTP leads to increase of charge carrier concentration. Additional lithium ions occupy the $Li(2)$ position and are expected to be more labile. Furthermore, additional lithium influences strongly the conductivity properties of the final LATP. Hence, in accordance with mentioned above and taking into account the visible conductivity fading and structural changes, we suspected to detect the $Li(2)$ polyhedron changes rather than $Li(1)$.

4.6. DFT calculated Li-ion positions, diffusion pathways and barriers

A computational study was started with the calculation of minimum energy path (MEP) related to a vacancy and interstitial migration mechanisms in pure parental LTP crystals (one Li^+ ion was removed or added to the cell respectively). The calculated vacancy diffusion barrier, 0.40 eV, agrees well with the experimental data for LTP [46] and previous theoretical works [24]. The calculated migration path goes through the $Li(2)$ position at (0.060, 0.306, 0.079) which is found to be the second most occupied position after the $Li(1)$ [47].

The calculated interstitial migration barrier (in LTP cell with one extra Li^+ ion) is only 0.15 eV which turned out to be slightly lower than the experimentally established bulk migration barrier (0.186 eV). This result confirms that the low migration barrier in LATP is mainly caused by simple addition of extra Li^+ ions (above the number of $Li(1)$ sites) rather than by some specific influence of Al atoms on the crystal structure. The minimal energy configuration along the MEP turned out to be a simultaneous occupation of two paired $Li(1/2)$ positions at (0.03047, 0.19973, 0.01903) (Fig. 7). This double-ion configuration will be denoted further as $Li(1/2) \times 2$. On the other hand, the $Li(2)$ position turned out to be the top point of the barrier (0.15 eV higher than the $Li(1/2) \times 2$ configuration).

Further, an energy landscape along the migration pathway was calculated using a long simulation cell including 4 consecutive $Li(1)$ position alternating with 4 $Li(2)$ positions (Fig. 7). The simulation cell in this case contained one Al atom replacing Ti. The number of Li^+ ions exceeded the number of $Li(1)$ sites by 1. That resulted in either occupation of one $Li(2)$ position or in $Li(1/2) \times 2$ configuration:

The Li^+ positions on the migration way are denoted as P0, P1 ... P8 (see Fig. 7; due to periodic boundary conditions the P8 position is equivalent to P0). The even positions (P0, P2 ...) represent an occupied $Li(2)$ position, while the odd ones (P1, P3 ...) represent the occupied $Li(1)$ or $Li(1/2)$ position depending on the absence or presence of the additional Li^+ ion at the moment of an imaginary Li^+ migration

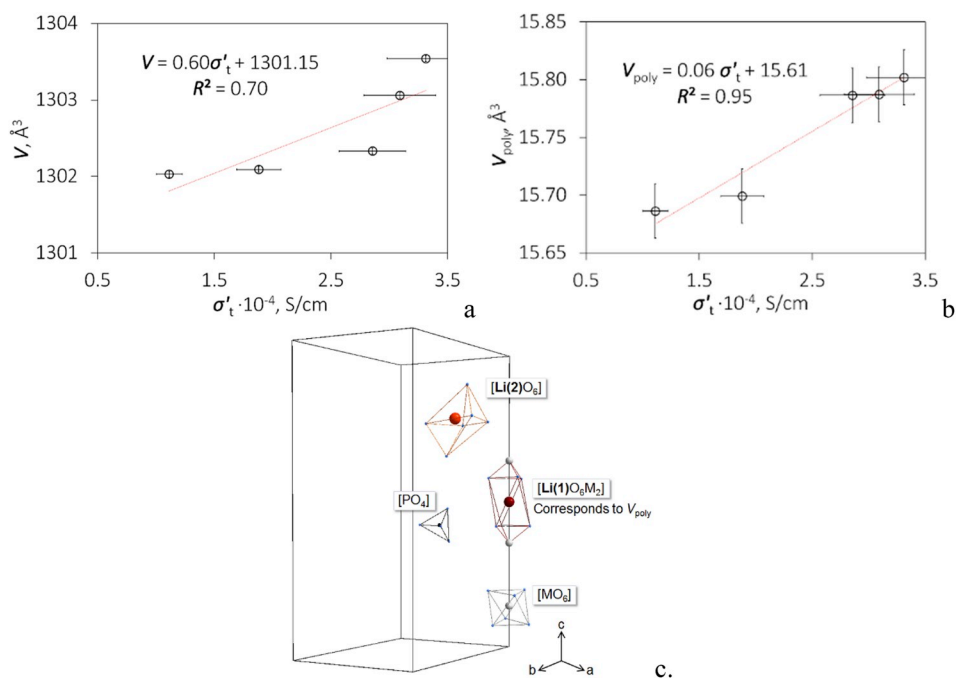


Fig. 6. The relationship of unit cell volume V (a) and intrastructural $[\text{Li}(1)\text{O}_6\text{M}_2]$ bi-pyramidal antiprism polyhedra volume V_{poly} (b) with approximate total conductivity σ'_T . All polyhedra discussed are shown in (c).

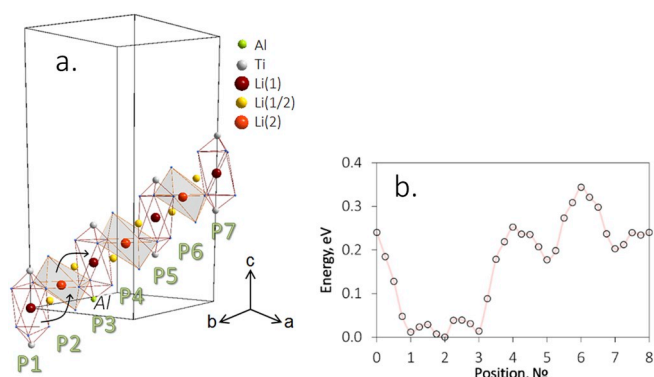


Fig. 7. The LATP Li-migration path described through the computational approach (a) and the energies of interstitial Li^+ migrating across a periodic cell ($\text{P}0 \rightarrow \text{P}8$) through the minimal energy path calculated via the NEB technique (b).

observation.

The calculated MEP is presented in Fig. 7b. There is a 0.25 eV trap around the Al atom, while outside the trap the migration barrier is about 0.15 eV (with $\text{Li}(1/2) \times 2$ configuration being the minimum) just as in case of interstitial migration of Li^+ in pure LTP. It should be noted that the energy difference between the $\text{Li}(1/2) \times 2$ configuration and the $\text{Li}(2)$ position occupation in the area near Al atom is less than 15 meV. This behavior may explain the $\text{Li}(2)$ occupation at room temperature.

4.7. DFT-modeling of the observed volume changes

As it was shown before, the LATP Li^+ migration path includes both $\text{Li}(1)$ and $\text{Li}(2)$ positions (Fig. 7). It was established, that moving along the migration path Li^+ ion upon entering the $\text{Li}(1)$ -polyhedron occupies one of the $\text{Li}(1/2)$ positions and pushes the ion that was originally resided in $\text{Li}(1)$ position to the other $\text{Li}(1/2)$ one forming the double-ion $\text{Li}(1/2) \times 2$ configuration. Thereby, one may expect that such $\text{Li}(1)$ -by- $\text{Li}(1/2) \times 2$ substitution will influence the $\text{Li}(1)$ -polyhedron volume V_{poly} .

That indeed can be concluded from Figure A19 (Supplementary, Section 17) that shows the calculated volumes of four $\text{Li}(1)$ -polyhedra located at the migration pathway (please, see Fig. 7) for different positions of the extra Li^+ ion. It is predicted that the $\text{Li}(1)$ -polyhedron expands upon the $\text{Li}(1)$ -by- $\text{Li}(1/2) \times 2$ configuration substitution and shrinks back through the opposite $\text{Li}(1/2) \times 2$ -by- $\text{Li}(1)$ substitution process.

The “breathing” V_{poly} behavior observed is consistent with in agreement with a steric hindrance point of view. The $\text{Li}(1)$ polyhedron, modeled in consideration with atomic sizes ($R_{\text{Ti}4+} = 0.60 \text{ \AA}$; $R_{\text{Al}3+} = 0.53 \text{ \AA}$; $R_{\text{Li}+} = 0.76 \text{ \AA}$; $R_{\text{O}2-} = 1.40 \text{ \AA}$; all for coordination number 6 [48]) is given in Fig. 8. It is seen, that one Li^+ ion at $\text{Li}(1)$ position is separated from oxygen ions with a gap, while two Li^+ ions in $\text{Li}(1/2) \times 2$ configuration have the lithium-oxygen contact in case of M and O(2) positions constancy (Fig. 8b). Thereby, we can conclude that the $\text{Li}(1)$ polyhedron expansion occurs due to the $\text{Li}(1/2) \times 2$ configuration substitution.

Hence, the overall shrinkage of $\text{Li}(1)$ polyhedron indicates a decrease of additional lithium content and, therefore, suggests that the Li-ion conductivity should diminish. This conclusion lays in line with the experimental results observed.

Previously the $\text{Li}(1/2) \times 2$ double-ion configuration was only predicted and described in Ref. [24], and still was not supported by experimental data. It is worth to emphasize, that the $\text{Li}(1/2) \times 2$ configuration was not originally used as a starting geometry in our calculations. Rather it was a result of geometry optimization of an intermediate point on the MEP Li^+ diffusion along the $\text{P}1 \rightarrow \text{P}8$ way. The direct experimental determination of the $\text{Li}(1/2)$ lithium position is a challenging task for both X-ray and neutron diffraction techniques. Thus

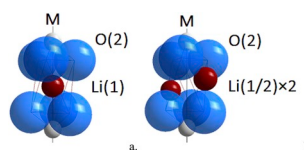


Fig. 8. The $\text{Li}(1)$ polyhedron represented with real ionic sizes: 1 Li^+ at $\text{Li}(1)$ position (a) and 2 Li^+ at $\text{Li}(1/2)$ positions — the $\text{Li}(1)$ -by- $\text{Li}(1/2) \times 2$ configuration (b).

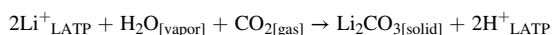
the signal of $\text{Li}(1/2) \times 2$ pair could be easily averaged to the $\text{Li}(1)$ position, that is right in the middle of the two $\text{Li}(1/2)$ ones. However, there is indirect descriptor of the $\text{Li}(1/2) \times 2$ pair occupation — the $\text{Li}(1)$ polyhedron volume V_{poly} . According to the geometry optimization results, the V_{poly} in case of $\text{Li}(1)$ configuration is 16.8 \AA^3 which is substantially smaller than for the $\text{Li}(1/2) \times 2$ occupation (17.7 \AA^3). The predicted relative volume decrease is about 5% while the experimental value does not exceed 1%. This discrepancy is resolved by taking into account the fact that the experimentally established V_{poly} obtained through the Rietveld refinement represents the value averaged upon the whole LATP crystal structure of the sample analyzed. Furthermore, the amount of extra lithium x in $\text{Li}_{1+x}\text{Al}_x\text{Ti}_{2-x}(\text{PO}_4)_3$ sample is less than 0.5, and it is also expected that some $\text{Li}(2)$ positions still should be occupied at room temperature.

4.8. Possible lithium-hydrogen substitution

In addition to the information given above, we found out that the V_{poly} decrease rate depends on the storage atmosphere. Namely, the aging in air atmosphere leads to the drastic decrease of V_{poly} in comparison with the aging in argon atmosphere (Table 1). Therefore, we consider the storage atmosphere composition as the main factor of degradation. Analyzing the differences of the ambient atmosphere and glovebox components, we noted two of them, which might interact with LATP: water (as humidity) and carbon dioxide. Thus, we may expect that the V_{poly} shrinkage is caused by the partial elimination of extra Li^+ ions out of the LATP structure. As a possible reason of such behavior the reaction of LATP ceramics with atmospheric components, such as H_2O , CO_2 , etc. can be proposed. In this case, we can assume that the degradation of LATP samples stored in a very clean low O_2 and H_2O ppm GloveBox proceeds much slower rate in comparison with the air-stored samples because of a far less concentration of these reactive species.

One may expect that LATP-air reaction may lead to the Li-by-H substitution. Therefore, additional geometry optimization calculations were performed to find equilibrium proton positions in the case of possible Li^+/H^+ exchange. For that purpose, one Li atom in the Al-containing simulation cell was replaced by a hydrogen atom. Both $\text{Li}(1)$ and $\text{Li}(2)$ positions turned out to be highly unfavorable for proton (in fact even local energy minimums were not found in these positions). In all cases, the optimization procedure resulted in a bonding between H and O atoms. The lowest energy configuration is characterized by H bonding with oxygen atom in O(2) position that is included in $[\text{AlO}_6]$ octahedron (the energy for the position connected to $[\text{TiO}_6]$ octahedron is about 0.1 eV higher). Thus upon Li^+/H^+ substitution facilitated by the reaction with air the total number of Li^+ ions decreases, while the total number of available sites (particularly, $\text{Li}(1)$) remains the same. As a result the $\text{Li}(1/2) \times 2$ configurations become rarer. That manifests in both decreased average V_{poly} and degraded total conductivity.

Due to the lithium lability and taking into account the structural and electrochemical changes observed, we can propose the following chemical reaction as a possible reason for the LATP degradation:



DFT calculations (Supplementary, Section 18) show that the energy balance of this reaction is close to zero within the accuracy of the theoretical model and uncertainty of reaction conditions. We expect, that the proposed lithium carbonate formation reaction takes place predominantly in the grain boundary areas as it requires fast flux of gaseous species. This degradation route would be in agreement with the observed prominent decrease of grain boundary conductivity.

5. Conclusions

This report is the first time that LATP ceramics degradation is characterized through the complex approach: different aspects such as

chemical composition, crystal structure, ion conductivity, and morphology were investigated using the wide range of analytical methods (EDX, PXRD, EIS, SEM) and the results obtained were supported by the DFT-based computations. It was shown, that simple two-step solid state synthesis allows synthesis of a pure α -NASICON-type LATP ceramic with satisfactory porosity of 18.5 vol% and high Li-ion total conductivity of $4 \cdot 10^{-4} \text{ S cm}^{-1}$ (room temperature). It was found out that the ceramics tend to degrade with measurable conductivity fading (σ_t , 76% for air and 28% for argon after 98 days) and crystal structure shrinkage. Additionally, bulk capacitance (C_b) of the pellets decreases up to 12 and 40% for argon- and air-stored samples. Approach to estimate the grain boundary layer thickness using C_b have been proposed. It was shown, that grain boundary thickness remains the same for the argon-stored sample, while for the air-stored one it increases twice which agrees with SEM-FIB data. The crystal structure - conductivity correlation was established through the investigation of intra-structural $\text{Li}(1)$ polyhedron and its volume V_{poly} , measured experimentally using the PXRD Rietveld refinement results and modeled atomistically at DFT level. It was proposed that the decrease of both conductivity and the polyhedron volume in the course of degradation is due to depletion of the extra Li^+ ions involved in low-barrier interstitial migration. The lithium consumption is assumed be the result of the reaction with air to form lithium carbonate. The theoretically predicted $\text{Li}(1/2) \times 2$ double-ion configuration was supported by the experimental evidences for the first time. The data obtained lays the foundation of the fresh view on the Li-ion migration mechanism, degradation processes, and the key influencers of crystal structure.

Declaration of competing interest

The authors declare that they have no known competing financial interests or personal relationships that could have appeared to influence the work reported in this paper.

Acknowledgments

The present work was supported by the Skoltech-MIT Next Generation Project “Lithium Redox Flow Batteries for High Power and High Energy Density Energy Storage”. Authors would like to express their gratitude to Dr. Jan Rohlicek, Dr. Michal Dusek, Dr. Vaclav Petricek, Department of Structure Analysis, Institute of Physics of the Czech Academy of Sciences, for helping us with the structure refinement settings; to Vadim Tarasyuk and Kirill Bulatov, Fablab of Skolkovo Institute of Science and Technology, for assisting us with the EIS cell prototyping; to Dr. Denis Sannikov, Timur Yagafarov, Center for Quantum Materials, Skolkovo Institute of Science and Technology, for assisting us with morphological SEM measurements and magnetron sputtering; to Dr. Artem Abakumov, Center for Energy Science and Technology, Skolkovo Institute of Science and Technology, for helping us with the FIB SEM measurements; to Dr. Stanislav Fedotov, Moscow State University, for helping us with the EDX measurements.

Appendix A. Supplementary data

Supplementary data to this article can be found online at <https://doi.org/10.1016/j.jpowsour.2019.227367>.

References

- [1] C.K. Chan, T. Yang, J. Mark Weller, Nanostructured garnet-type $\text{Li}_7\text{La}_3\text{Zr}_2\text{O}_{12}$: synthesis, properties, and opportunities as electrolytes for Li-ion batteries, *Electrochim. Acta* 253 (2017) 268–280, <https://doi.org/10.1016/j.electacta.2017.08.130>.
- [2] J.B. Goodenough, H.Y.P. Hong, J.A. Kafalas, K. Dwight, report Solid Electrolytes: Alkali-Ion Transport in Skeleton Structures. Semiannual Technical Summary Report, 1 Jan–30 Jun 1976. [Na/sub 3/Zr/sub 2/Si/sub 2/PO/sub 12/and K/sub 1/sub 9/Mg/sub 0/sub 95/Si/sub 1/sub 05/O/sub 4/], (n.d.).

- [3] H. SCHMID, L. DEJONGHE, C. CAMERON, Chemical stability of nasicon, *Solid State Ion.* 6 (1982) 57–63, [https://doi.org/10.1016/0167-2738\(82\)90096-0](https://doi.org/10.1016/0167-2738(82)90096-0).
- [4] H.Y.P. Hong, J.B. Goodenough, Compositions for Fast Alkali-Metal-Ion Transport, 1977.
- [5] F. Zheng, M. Kotobuki, S. Song, M.O. Lai, L. Lu, Review on solid electrolytes for all-solid-state lithium-ion batteries, *J. Power Sources* 389 (2018) 198–213, <https://doi.org/10.1016/j.jpowsour.2018.04.022>.
- [6] A. Rossbach, F. Tietz, S. Griesshammer, Structural and transport properties of lithium-conducting NASICON materials, *J. Power Sources* 391 (2018) 1–9, <https://doi.org/10.1016/j.jpowsour.2018.04.059>.
- [7] E. Zhao, F. Ma, Y. Guo, Y. Jin, Stable LATP/LAGP double-layer solid electrolyte prepared via a simple dry-pressing method for solid state lithium ion batteries, *RSC Adv.* 6 (2016) 92579–92585, <https://doi.org/10.1039/C6RA19415J>.
- [8] Z. Jian, Y.-S. Hu, X. Ji, W. Chen, NASICON-structured materials for energy storage, *Adv. Mater.* 29 (2017) 1601925, <https://doi.org/10.1002/adma.201601925>.
- [9] M.M. Ioanniti, W.E. Tenhaeff, Enhancing the stability of lithium ion $\text{Li}_{1+x-y}\text{Al}_x\text{Ti}_{2-x}\text{Si}_y\text{P}_{3-y}\text{O}_{12}$ glass – ceramic conductors in aqueous electrolytes, *J. Power Sources* 371 (2017) 209–216, <https://doi.org/10.1016/j.jpowsour.2017.10.040>.
- [10] H. Xu, S. Wang, H. Wilson, F. Zhao, A. Manthiram, Y-doped NASICON-type $\text{LiZr}_2(\text{PO}_4)_3$ Solid electrolytes for lithium-metal batteries, *Chem. Mater.* 29 (2017) 7206–7212, <https://doi.org/10.1021/acs.chemmater.7b01463>.
- [11] N. Bounar, A. Benabbas, P. Ropa, J.-C. Carru, Synthesis and ionic conductivity of NASICON - structured $\text{LiTi}_{2-x}\text{Sn}_x(\text{PO}_4)_3$ anode material for lithium - ion batteries, *Adv. Mater. Process. Technol.* 3 (2017) 241–249, <https://doi.org/10.1080/2374068X.2016.1247231>.
- [12] S. Smith, T. Thompson, J. Sakamoto, J.L. Allen, D.R. Baker, J. Wolfenstine, Electrical, mechanical and chemical behavior of $\text{Li}_{1.2}\text{Zr}_{1.9}\text{Sr}_{0.1}(\text{PO}_4)_3$, *Solid State Ion.* 300 (2017) 38–45, <https://doi.org/10.1016/j.ssi.2016.11.032>.
- [13] B. Mandal, A.K. Thakur, AC Impedance Spectroscopy of NASICON Type $\text{Na}_3\text{Fe}_2(\text{PO}_4)_3$ Ceramic, 2018, 050018, <https://doi.org/10.1063/1.5032673>.
- [14] M. Catti, S. Stramare, Lithium location in NASICON-type Li^+ -conductors by neutron diffraction: II. Rhombohedral $\alpha\text{-LiZr}_2(\text{PO}_4)_3$ at $T = 423\text{ K}$, *Solid State Ion.* 136 (2000) 489–494, [https://doi.org/10.1016/S0167-2738\(00\)00459-8](https://doi.org/10.1016/S0167-2738(00)00459-8).
- [15] P. Zhang, H. Wang, Y.-G. Lee, M. Matsui, Y. Takeda, O. Yamamoto, N. Imanishi, Tape-cast water-stable NASICON-type high lithium ion conducting solid electrolyte films for aqueous lithium-air batteries, *J. Electrochem. Soc.* 162 (2015) A1265–A1271, <https://doi.org/10.1149/2.0711507jes>.
- [16] M. Tang, H. Wang, Y.-G. Lee, Y. Takeda, O. Yamamoto, J. Xu, A. Yuan, N. Imanishi, Lithium-stable high lithium ion conducting $\text{Li}_{1.4}\text{Al}_{0.4}\text{Ge}_{0.2}\text{Ti}_{1.4}(\text{PO}_4)_3$ solid electrolyte, *J. Electrochem. Soc.* 163 (2016) A1822–A1828, <https://doi.org/10.1149/2.0121609jes>.
- [17] K. Arbi, W. Bucheli, R. Jiménez, J. Sanz, High lithium ion conducting solid electrolytes based on NASICON $\text{Li}_{1+x}\text{Al}_x\text{M}_{2-x}(\text{PO}_4)_3$ materials ($\text{M} = \text{Ti}, \text{Ge}$ and $0 \leq x \leq 0.5$), *J. Eur. Ceram. Soc.* 35 (2015) 1477–1484, <https://doi.org/10.1016/j.jeurceramsoc.2014.11.023>.
- [18] H. Aono, E. Sugimoto, Y. Sadaoka, N. Imanaka, G. Adachi, Ionic conductivity of the lithium titanium phosphate ($\text{Li}_{1+x}\text{M}_x\text{Ti}_{2-x}(\text{PO}_4)_3$, $\text{M} = \text{Al}, \text{Sc}, \text{Y}$, and La) systems, *J. Electrochem. Soc.* 136 (1989) 590–591, <https://doi.org/10.1149/1.2096693>.
- [19] L. Yang, Z. Wang, Y. Feng, R. Tan, Y. Zuo, R. Gao, Y. Zhao, L. Han, Z. Wang, F. Pan, Flexible composite solid electrolyte facilitating highly stable “soft contacting” Li^+ -electrolyte interface for solid state lithium-ion batteries, *Adv. Energy Mater.* 7 (2017) 1–9, <https://doi.org/10.1002/aenm.201701437>.
- [20] M. Pérez-Estébanez, J. Isasi-Marín, D.M. Többsen, A. Rivera-Calzada, C. León, A systematic study of Nasicon-type $\text{Li}_{1+x}\text{M}_x\text{Ti}_{2-x}(\text{PO}_4)_3$ ($\text{M} = \text{Cr}, \text{Al}, \text{Fe}$) by neutron diffraction and impedance spectroscopy, *Solid State Ion.* 266 (2014) 1–8, <https://doi.org/10.1016/j.ssi.2014.07.018>.
- [21] T. Hupfer, E.C. Bucharsky, K.G. Schell, A. Senyshyn, M. Monchak, M.J. Hoffmann, H. Ehrenberg, Evolution of microstructure and its relation to ionic conductivity in $\text{Li}_{1+x}\text{Al}_x\text{Ti}_{2-x}(\text{PO}_4)_3$, *Solid State Ion.* 288 (2016) 235–239, <https://doi.org/10.1016/j.ssi.2016.01.036>.
- [22] Y. Wang, W.D. Richards, S.P. Ong, L.J. Miara, J.C. Kim, Y. Mo, G. Ceder, Design principles for solid-state lithium superionic conductors, *Nat. Mater.* 14 (2015) 1026–1031, <https://doi.org/10.1038/nmat4369>.
- [23] X. He, Y. Zhu, Y. Mo, Origin of fast ion diffusion in super-ionic conductors, *Nat. Commun.* 8 (2017) 15893, <https://doi.org/10.1038/ncomms15893>.
- [24] B. Lang, B. Ziebarth, C. Elsässer, Lithium ion conduction in $\text{LiTi}_2(\text{PO}_4)_3$ and related compounds based on the NASICON structure: a first-principles study, *Chem. Mater.* 27 (2015) 5040–5048, <https://doi.org/10.1021/acs.chemmater.5b01582>.
- [25] M. Dusek, V. Petricek, L. Palatinus, Program for Structure Analysis of Crystals Periodic in Three or More Dimensions from Diffraction Data - Jana2006, ((n.d.)).
- [26] S.R. Material, NIST Certificate of Analysis: SRM 676a (2015) 1–7.
- [27] G.J. Redhammer, D. Rettenwander, S. Pristat, E. Dashjav, C.M.N. Kumar, D. Topa, F. Tietz, A single crystal X-ray and powder neutron diffraction study on NASICON-type $\text{Li}_{1+x}\text{Al}_x\text{Ti}_{2-x}(\text{PO}_4)_3$ ($0 \leq x \leq 0.5$) crystals: implications on ionic conductivity, *Solid State Sci.* 60 (2016) 99–107, <https://doi.org/10.1016/j.solidstatesciences.2016.08.011>.
- [28] The FreeCad software official Web page (n.d.), <https://www.freecadweb.org/>.
- [29] G. Kresse, J. Furthmüller, Efficient iterative schemes for ab initio total-energy calculations using a plane-wave basis set, *Phys. Rev. B* 54 (1996) 11169–11186, <https://doi.org/10.1103/PhysRevB.54.11169>.
- [30] J.P. Perdew, K. Burke, M. Ernzerhof, Generalized gradient approximation made simple, *Phys. Rev. Lett.* 77 (1996) 3865–3868, <https://doi.org/10.1103/PhysRevLett.77.3865>.
- [31] P.E. Blöchl, Projector augmented-wave method, *Phys. Rev. B* 50 (1994) 17953–17979, <https://doi.org/10.1103/PhysRevB.50.17953>.
- [32] G. Mills, H. Jónsson, G.K. Schenter, Reversible work transition state theory: application to dissociative adsorption of hydrogen, *Surf. Sci.* 324 (1995) 305–337, [https://doi.org/10.1016/0039-6028\(94\)00731-4](https://doi.org/10.1016/0039-6028(94)00731-4).
- [33] D.A. Aksyonov, S.S. Fedotov, K.J. Stevenson, A. Zhugayevych, Understanding migration barriers for monovalent ion insertion in transition metal oxide and phosphate based cathode materials: a DFT study, *Comput. Mater. Sci.* 154 (2018) 449–458, <https://doi.org/10.1016/j.commatsci.2018.07.057>.
- [34] F. Shan, V.A. Couch, T. Guo, Atomic tungsten for ultrafast hard X-ray generation, *J. Phys. Chem. A* 109 (2005) 4216–4220, <https://doi.org/10.1021/jp0511810>.
- [35] I.M. Hodge, M.D. Ingram, A.R. West, Impedance and modulus spectroscopy of polycrystalline solid electrolytes, *J. Electroanal. Chem. Interfacial Electrochem.* 74 (1976) 125–143, [https://doi.org/10.1016/S0022-0728\(76\)80229-X](https://doi.org/10.1016/S0022-0728(76)80229-X).
- [36] P.E. Kazin, A.S. Karpov, M. Jansen, J. Nuss, Y.D. Tretyakov, Crystal structure and properties of strontium phosphate apatite with oxocuprate ions in hexagonal channels, *Z. Anorg. Allg. Chem.* 629 (2003) 344–352, <https://doi.org/10.1002/zaac.200390055>.
- [37] K. Arbi, S. Mandal, J.M. Rojo, J. Sanz, Dependence of ionic conductivity on composition of fast ionic conductors $\text{Li}_{1+x}\text{Ti}_{2-x}\text{Al}_x(\text{PO}_4)_3$, $0 \leq x \leq 0.7$. A parallel NMR and electric impedance study, *Chem. Mater.* 14 (2002) 1091–1097, <https://doi.org/10.1021/cm010528i>.
- [38] C.R. Mariappan, M. Gellert, C. Yada, F. Rosciano, B. Roling, Grain boundary resistance of fast lithium ion conductors: comparison between a lithium-ion conductive Li-Al-Ti-P-O -type glass ceramic and a $\text{Li}_{1.5}\text{Al}_{0.5}\text{Ge}_{1.5}\text{P}_{3.0}\text{O}_{12}$ ceramic, *Electrochem. Commun.* 14 (2012) 25–28, <https://doi.org/10.1016/j.elecom.2011.10.022>.
- [39] J.S. Thokchom, B. Kumar, The effects of crystallization parameters on the ionic conductivity of a lithium aluminum germanium phosphate glass-ceramic, *J. Power Sources* 195 (2010) 2870–2876, <https://doi.org/10.1016/j.jpowsour.2009.11.037>.
- [40] S. Duluard, A. Paillassa, L. Puech, P. Vinatier, V. Turq, P. Rozier, P. Lenormand, P. L. Taberna, P. Simon, F. Ansart, Lithium conducting solid electrolyte $\text{Li}_{1.3}\text{Al}_{0.3}\text{Ti}_{1.7}(\text{PO}_4)_3$ obtained via solution chemistry, *J. Eur. Ceram. Soc.* 33 (2013) 1145–1153, <https://doi.org/10.1016/j.jeurceramsoc.2012.08.005>.
- [41] P. Hartmann, T. Leichtweiss, M.R. Busche, M. Schneider, M. Reich, J. Sann, P. Adelhelm, J. Janek, Degradation of NASICON-type materials in contact with lithium metal: formation of mixed conducting interphases (MCI) on solid electrolytes, *J. Phys. Chem. C* 117 (2013) 21064–21074, <https://doi.org/10.1021/jp4051275>.
- [42] J.E. Bauerle, Study of solid electrolyte polarization by a complex admittance method, *J. Phys. Chem. Solids* 30 (1969) 2657–2670, [https://doi.org/10.1016/0022-3697\(69\)90039-0](https://doi.org/10.1016/0022-3697(69)90039-0).
- [43] J. Fu, Superionic conductivity of glass-ceramics in the system $\text{Li}_2\text{O}-\text{Al}_2\text{O}_3-\text{TiO}_2-2\text{P}_2\text{O}_5$, *Solid State Ion.* 96 (1997) 195–200, [https://doi.org/10.1016/S0167-2738\(97\)00018-0](https://doi.org/10.1016/S0167-2738(97)00018-0).
- [44] L. Hallopeau, D. Bregiroux, G. Rousse, D. Portehault, P. Stevens, G. Toussaint, C. Laberty-Robert, Microwave-assisted reactive sintering and lithium ion conductivity of $\text{Li}_{1.3}\text{Al}_{0.3}\text{Ti}_{1.7}(\text{PO}_4)_3$ solid electrolyte, *J. Power Sources* 378 (2018) 48–52, <https://doi.org/10.1016/j.jpowsour.2017.12.021>.
- [45] T. van Dijk, A.J. Burggraaf, Grain boundary effects on ionic conductivity in ceramic $\text{Gd}_x\text{Zr}_{1-x}\text{O}_{2-(x/2)}$ solid solutions, *Phys. Status Solidi* 63 (1981) 229–240, <https://doi.org/10.1002/pssa.2210630131>.
- [46] K. Arbi, J.M. Rojo, J. Sanz, Lithium mobility in titanium based Nasicon $\text{Li}_{1+x}\text{Ti}_{2-x}\text{Al}_x(\text{PO}_4)_3$ and $\text{LiTi}_2-x\text{Zr}_x(\text{PO}_4)_3$ materials followed by NMR and impedance spectroscopy, *J. Eur. Ceram. Soc.* 27 (2007) 4215–4218, <https://doi.org/10.1016/j.jeurceramsoc.2007.02.118>.
- [47] M. Monchak, T. Hupfer, A. Senyshyn, H. Boysen, D. Chernyshov, T. Hansen, K. G. Schell, E.C. Bucharsky, M.J. Hoffmann, H. Ehrenberg, Lithium diffusion pathway in $\text{Li}_{1.3}\text{Al}_{0.3}\text{Ti}_{1.7}(\text{PO}_4)_3$ (LATP) superionic conductor, *Inorg. Chem.* 55 (2016) 2941–2945, <https://doi.org/10.1021/acs.inorgchem.5b02821>.
- [48] R.D. Shannon, Revised effective ionic radii in halides and chalcogenides, *Acta Crystallogr.* (1976) 751, <https://doi.org/10.1107/S0567739476001551>.